

Numerical comparison between a Gyrofluid and Gyrokinetic model investigating collisionless magnetic reconnection

O. Zacharias¹, L. Comisso^{2,3}, D. Grasso^{2,3}, R. Kleiber¹, M. Borchardt¹ and R. Hatzky⁴

¹ IPP-Teilinstitut Greifswald, Wendelsteinstr. 1, D-17491 Greifswald, Germany

² Dipartimento Energia, Politecnico di Torino, Corso Duca degli Abruzzi 24, 10129, Torino, Italy

³ Istituto dei Sistemi Complessi - CNR, Via dei Taurini 19, 00185, Roma, Italy

⁴ Max-Planck-Institut für Plasmaphysik, Boltzmannstr. 2, 85748 Garching, Germany

Abstract

The first detailed comparison between gyrokinetic and gyrofluid simulations of collisionless magnetic reconnection has been carried out. Both the linear and nonlinear evolution of the collisionless tearing mode have been analyzed. In the linear regime, we have found a good agreement between the two approaches over the whole spectrum of linearly unstable wave numbers, both in the drift kinetic limit and for finite ion temperature. Nonlinearly, focusing on the small- Δ' regime, with Δ' indicating the standard tearing stability parameter, we have compared relevant observables such as the evolution and saturation of the island width, as well as the island oscillation frequency in the saturated phase. The results are basically the same, with small discrepancies only in the value of the saturated island width for moderately high values of Δ' . Therefore, in the regimes investigated here, the gyrofluid approach can describe the collisionless reconnection process as well as the more complete gyrokinetic model.

PACS numbers: 52.35.Vd, 52.35.Py, 52.25.Dg, 52.65.Kj, 52.65.Tt, 52.65.Rr

Keywords: magnetic reconnection, gyrofluid and gyrokinetic simulations, plasma kinetic theory, plasma fluid theory

I. INTRODUCTION

Reconnection of magnetic fields is recognized to play a key role in many events occurring in laboratory, space, and astrophysical plasmas. Classical examples of such events are sawtooth crashes in tokamaks, substorms in the Earth's Magnetosphere, and solar flares. Magnetic reconnection involves a topology change of a set of field lines, which leads to a new equilibrium configuration with lower magnetic energy. During this process magnetic energy is converted into kinetic and thermal energy of electrons and ions [1]. Although much of the progress in the understanding of magnetic reconnection has been possible thanks to the use of fluid-based models, the results achieved with these models require independent confirmation when kinetic effects are expected to be important.

Recently, a new class of generalized fluid models, so called gyrofluid models, have been adopted to investigate magnetic reconnection in the presence of a large guide field [2–10]. These models combine the advantages of the fluid description, namely computational efficiency and intuitively appealing physical interpretation, while retaining important kinetic effects through gyro-orbit averaging [11]. However, for problems in which strongly non-Maxwellian features characterize the distribution function it would probably be necessary to keep many velocity-space moments to describe the detailed shape of the distribution function, in which case the gyrofluid approach may lose its advantages [12]. Therefore, detailed comparisons between gyrokinetic and gyrofluid simulations are necessary to confirm the validity of the continuum gyrofluid descriptions and to improve them when such descriptions are no longer applicable.

An early investigation of collisionless tearing modes by means of gyrokinetic particle-in-cell (PIC) simulations was made in Ref. [13]. In particular, this work focused on the growth and nonlinear evolution of small-scale magnetic islands having a characteristic width of the order of the electron skin depth and smaller than the ion Larmor radius. In Ref. [14] the evolution of collisionless and semicollisional tearing mode instabilities was studied using a gyrokinetic δf PIC code with gyrokinetic ions and drift-kinetic electrons. After a bench-

mark of the linear simulation results with eigenmode analysis for the case of fixed ions, the nonlinear evolution of the magnetic island width was calculated. More recently, in Ref. [15] numerical results of saturated island widths resulting from gyrokinetic δf PIC simulations were compared to analytical calculations [16] in a more extended parameter space. In this work electron diamagnetic effects were also considered, and it was found that they have stabilizing effects in agreement with the asymptotic theory of Ref. [17]. Simulations of the collisionless tearing mode with gyrokinetic electrons and fully kinetic ions were performed in Ref. [18] and compared with the asymptotic matching theory of Ref. [16], and with a gyrokinetic eigenmode theory in a small but finite Larmor radius limit. Very recently, collisionless reconnection in the large guide field regime has also been investigated by comparing fully kinetic PIC simulations and gyrokinetic results, showing that the gyrokinetic framework is capable of making accurate predictions well outside its formal regime of applicability [19]. It was also shown that many physical quantities resulting from the nonlinear reconnection process scale linearly with the guide field.

The first comparison between gyrokinetic and fluid simulations was carried out in Ref. [20, 21], where both the linear and nonlinear regimes of collisionless magnetic reconnection were investigated, finding a reasonably good agreement between the two approaches for low- β plasmas and small ion to electron temperature ratio. For $\beta \sim 1$ and ion temperature greater than the electron temperature, an increase in discrepancy between gyrokinetic simulations and fluid theory was found in Ref. [22], where, however, it was shown that the adoption of a reduced ion-to-electron mass ratio plays a significant role in causing these discrepancies. This latter work focused on the linear regime, but also considered the collisionality dependence of the tearing mode growth. The importance of adopting a realistic mass ratio was emphasized in Ref. [23], where extensive linear studies were presented, and nonlinear results were performed to investigate reconnection in the cases of decaying and driven turbulence. As in most of the works mentioned above, in this paper we focus on rarefied high-temperature plasmas in which the collisional mean free path is large enough that collisions are negligible. Additionally we consider magnetic reconnection phenomena that take place in a two-

dimensional plane perpendicular to a strong and constant magnetic guide field. Differently from previous studies, here the comparison is between the results of gyrokinetic and gyrofluid simulations. For this purpose, we adopt the gyrokinetic δf PIC code EUTERPE with gyrokinetic ions and drift-kinetic electrons [15]. Recently, a linear version of this code (GYGLES) has been employed to simulate the ideal-MHD internal kink mode and the collisionless $m = 1$ tearing mode in a tokamak [24]. We also adopt the gyrofluid code that has been employed in Refs. [7, 9, 10] to investigate ion gyro-orbit averaging effects on collisionless magnetic reconnection. After a linear benchmark of these codes with a numerical eigenmode and eigenvalue analysis, the results of the two models in the linear regime are compared over the whole spectrum of linearly unstable wave numbers, both in the drift kinetic limit and for finite ion temperature. Nonlinearly, focusing on the small Δ' regime (with Δ' indicating the standard tearing stability parameter), we compare relevant observables as the evolution and saturation of the island half-width, and the island oscillation frequency at saturation.

This paper is organized as follows: In Sec. II the adopted gyrokinetic and gyrofluid models are described, as well as the initial equilibrium configuration. In Sec. III we focus on linear simulation results, while the nonlinear regime is studied in Sec. IV. Finally, in Sec. V we summarize our results and discuss their implications.

II. THE MODELS

Within the framework of low- β plasmas, $\beta \ll 1$, the dominant field fluctuations are the electrostatic potential $\hat{\Phi}$ and the parallel vector potential \hat{A}_{\parallel} . Both models which are investigated here adopt the following normalization scheme with respect to Alfvén units

$$t = \frac{v_A}{L} \hat{t}, \quad x = \frac{\hat{x}}{L}, \quad d_s = \frac{\hat{d}_s}{L}, \quad \rho_{s,e} = \frac{\hat{\rho}_{s,e}}{L}, \quad (1)$$

$$n_s = \frac{L \hat{n}_s}{\hat{d}_i n_0}, \quad u_s = \frac{L \hat{u}_s}{\hat{d}_i v_A}, \quad A = \frac{\hat{A}_{\parallel}}{B_{0,z} L}, \quad \Phi = \frac{\hat{\Phi}}{B_{0,z} L v_A} \quad (2)$$

where the carets denote the dimensional quantities, u_s is the out-of-plane guiding center velocity field, n_s is the guiding center density perturbation, and a constant background density n_0 is assumed to be equal for each species s . L indicates a characteristic magnetic

equilibrium length scale, while $v_A = B_{0,z}/\sqrt{\mu_0 n_0 m_i}$ is the Alfvén speed based on the magnetic field strength $B_{0,z}$ of the guiding field. $\hat{d}_s = c/\omega_{p,s}$ is the skin depth of singly charged ions ($s = 1$) or electrons ($s = 2$) and $\rho_{S,e} = \sqrt{m_i k_B T_{0,e}}/(e B_{0,z})$ is the sound Larmor radius. The ratio of ion temperature $T_{0,i}$ to the reference temperature of the electrons $T_{0,e}$ is indicated by τ , while μ refers to the ratio of the ions mass m_i to electron mass m_e . Also, the electron plasma- β is defined by $\beta_e = \mu_0 k_B T_{0,e} n_0/B_{0,z}^2$, whereas $\beta_i = \beta_e \tau$ for ions.

A. The gyrokinetic model

The particle-in-cell code EUTERPE [25] uses a δf -scheme splitting of the distribution function f_s for each species s into a time independent background $f_{0,s}$ and a perturbed part δf_s in order to solve the full standard gyrokinetic Vlasov-Maxwell-system [27] globally in toroidal 3D-geometry. Here the code is modified to simulate the tearing mode in slab geometry. The background distribution function is assumed to be a shifted Maxwellian with bulk velocity $u_{0,s}$. EUTERPE works in the p_{\parallel} -formalism so that the equations for particles trajectories are in a slab geometry [26, 27]

$$\dot{\vec{R}}_s = \frac{1}{\alpha \sqrt{\beta_e} m_s} p_{\parallel} \vec{b} - \Omega_s A \vec{b} + \vec{b} \times \nabla \langle \Psi \rangle \quad (3)$$

$$= \frac{1}{\alpha \sqrt{\beta_e} m_s} p_{\parallel} \vec{b} + \dot{\vec{R}}_s^1 \quad (4)$$

$$\frac{\dot{p}_{\parallel,s}}{m_s} = -\alpha \sqrt{\beta_e} \Omega_s \vec{b} \cdot \nabla \langle \Psi \rangle, \quad (5)$$

where $\Omega_s = (q_s B_{0,z}/m_s) L/v_A$ is the cyclotron frequency normalized to the Alfvén time for each species, q_s is the species charge, $\Psi = \Phi - A p_{\parallel}/m_s$, \vec{b} is the normalized magnetic field and $\alpha = L/\rho_{S,e}$. The perturbed distribution function is pushed along the particle orbits according to

$$\delta \dot{f}_s = -\dot{f}_{0,s} \quad (6)$$

$$= -f_{0,s} \left(\kappa_{u_{0,s}} \dot{\vec{R}}_s^1 \cdot \nabla x + \frac{\Omega_s \sqrt{\beta_e} \alpha}{v_s^2} \left(\frac{p_{\parallel}}{m_s} - u_{0,s} \right) \vec{b} \cdot \nabla \langle \Psi \rangle \right). \quad (7)$$

The current gradient term with the bulk velocity $u_{0,s}$ reads

$$\kappa_{u_{0,s}}(x) = \frac{\frac{p_{\parallel}}{m_s} - u_{0,s}}{v_s^2} \frac{du_{0,s}}{dx}$$

and $v_s = \sqrt{k_B T_s / m_s} / (v_A \hat{d}_i / L)$ is the normalized thermal speed of each species. The quasineutrality condition for drift kinetic electrons and gyrokinetic ions reads

$$n_e = \langle n_i \rangle + \frac{\Gamma_0 - 1}{\rho_i^2} \Phi. \quad (8)$$

Γ_0 is an integral operator that describes the average of the electrostatic potential over a gyro-ring around the guiding center position. If necessary the polarization density is approximated by a Padé approximation due to the relative complex structure of Γ_0 in real space. Otherwise the ion response is simplified by using a long wavelength approximation, $k_{\perp}^2 \rho_i^2 \ll 1$. Expanding $\Gamma_0 - 1$ in a Taylor series in this limit, the quasineutrality condition becomes

$$n_e = \langle n_i \rangle + \nabla_{\perp}^2 \Phi. \quad (9)$$

The gyroaveraging of the ion guiding center density perturbation, n_i , can be expressed by the phase space integral

$$\langle n_i \rangle(\vec{x}) = \int J d^6 Z \delta(\vec{R} + \vec{\rho}_i - \vec{x}) \delta f_i \quad (10)$$

with the phase space Jacobian $J = B$, $d^6 Z = d\vec{R} (dp_{\parallel} / m_i) v_{\perp} dv_{\perp} d\alpha$ and the gyroradius vector $\vec{\rho}_i(\alpha)$.

Ampère's law closes the Vlasov-Maxwell-system

$$-\nabla_{\perp}^2 A + \sum_s \frac{\beta_s}{\rho_s^2} A = \sum_s \langle j_{\parallel,s} \rangle \quad (11)$$

with the Larmor radii $\rho_s = \sqrt{m_s k_B T_s} / (e B_{0,z})$ for each species. The corresponding gyroaveraged "current" response is calculated according to

$$\langle j_{\parallel,i} \rangle(\vec{x}) = \int J d^6 Z \delta(\vec{R} + \vec{\rho}_i - \vec{x}) \frac{p_{\parallel}}{m_i} \delta f_i. \quad (12)$$

The gyroaveraging procedure of the fields A, Φ is being employed according to

$$\langle A, \Phi \rangle(\vec{R}) = \frac{1}{2\pi} \int (A, \Phi)(\vec{R} + \vec{\rho}) d\alpha, \quad (13)$$

taking sufficiently many points on the gyro ring around the guiding center position \vec{R} . Recently, serious computational difficulties concerning the skin terms in Eq. (11) could be resolved using an enhanced control variate method [28].

B. The gyrofluid model

We consider the gyrofluid model that has been adopted in Refs. [7, 9, 10] to investigate magnetic reconnection in collisionless high-temperature plasmas with a strong guide field. This model is obtained from the equations of Ref. [32] by neglecting magnetic curvature effects and assuming two-dimensional dynamics with $\partial/\partial z = 0$, being z the direction of the strong guide field. In turn, the model of Ref. [32] was obtained from the equations of Ref. [33] by taking only the first two velocity space moments of the gyrokinetic equations for both the electrons and the ions, assuming constant temperatures and neglecting collisions and the electron gyroradius. Electron inertia terms, on the other hand, were retained in order to break the frozen-in condition and allow for magnetic reconnection phenomena. Therefore, the evolution equations of this gyrofluid model consist of the continuity equation and the z -component of the equation of motion for the ion guiding centers:

$$\frac{\partial n_i}{\partial t} + [\Gamma_0^{1/2} \Phi, n_i] = [u_i, \Gamma_0^{1/2} A], \quad (14)$$

$$\frac{\partial D}{\partial t} + [\Gamma_0^{1/2} \Phi, D] = \tau \rho_{S,e}^2 [\Gamma_0^{1/2} A, n_i], \quad (15)$$

and similar equations for the electrons:

$$\frac{\partial n_e}{\partial t} + [\Phi, n_e] = [u_e, A], \quad (16)$$

$$\frac{\partial F}{\partial t} + [\Phi, F] = -\rho_{S,e}^2 [A, n_e], \quad (17)$$

where the Poisson brackets between two generic fields f and g are defined by $[f, g] = \vec{z} \cdot \nabla f \times \nabla g$. Here $D = \Gamma_0^{1/2} A + d_i^2 u_i$ is the ion guiding center parallel canonical momentum, whereas $F = A - d_e^2 u_e$ is the electron parallel canonical momentum. Furthermore, $\Gamma_0^{1/2} \Phi$ is the gyro-averaged electrostatic potential and $\Gamma_0^{1/2} A$ is the gyro-averaged parallel magnetic potential, where the symbol $\Gamma_0^{1/2}$ refers to the gyro-averaging operator that we adopt in its lowest-order Padé approximant form [12]

$$\Gamma_0^{1/2} = \frac{1}{1 - \frac{\rho_i^2}{2} \nabla_\perp^2}. \quad (18)$$

This approximation gives reasonable values for the whole range of $k_\perp^2 \rho_i^2$. The system of equations is completed by the parallel component of Ampère's law,

$$\nabla_\perp^2 A = u_e - \Gamma_0^{1/2} u_i \quad (19)$$

and by the quasineutrality condition

$$n_e = \Gamma_0^{1/2} n_i + \frac{\Gamma_0 - 1}{\rho_i^2} \Phi. \quad (20)$$

The resulting model is dissipationless and suitable for the study of reconnection mediated by electron inertia. In particular, it possesses a noncanonical Hamiltonian structure [32] that reveals the presence of four Lagrangian invariants, which have proved to be helpful to understand how the reconnection evolution is affected by the plasma β and by the ratio of species temperatures [7, 10].

C. Equilibrium configuration and numerical setup

To investigate spontaneous reconnection, the model equations are solved numerically with an initial equilibrium that is unstable with respect to tearing modes. The instability reconnects the antiparallel component of magnetic field lines at the resonant surface defined by $\vec{k} \cdot \vec{B}_0 = 0$, with \vec{k} indicating the wavevector of the mode. We consider a two-dimensional slab geometry with x as the coordinate of the equilibrium inhomogeneity and setting $\partial/\partial z = 0$. The equilibrium magnetic field \vec{B}_0 results from an equilibrium current $u_{0,e}$ carried by

electrons only (for ions $u_{0,i} = 0$). The perpendicular sheared magnetic field can be deduced from a parallel vector potential $A_{0,\parallel}(x)$, which is chosen to be

$$A_{0,\parallel}(x) = \frac{C}{\cosh^2(x)}. \quad (21)$$

The parameter C was chosen to be $C = 0.1$ if not stated otherwise. This results in a maximal relative shear strength of $B_{0,y}/B_{0,z} \sim 0.08$ in the domain and a shear length $l_s = B_{0,z}/(dB_{0,y}/dx) = 5$ at the resonant surface $x = 0$.

Furthermore, the plasma is considered homogeneous with flat density $n_{0,s}(x) = n_{\text{eq}}$ and temperature profiles $T_{0,s}(x) = T_{0,s}$ for every species s . We considered a simulation domain $\{(x, y) : -\pi \leq x \leq \pi, -a\pi \leq y \leq a\pi\}$, where the parameter a fixes the domain length L_y in y -direction, which is linked to the wavenumber $k_y = 2\pi m/L_y$ of the longest wavelength mode $m = 1$ of the system. The tearing mode stability quantity [29] Δ' is then characterized by the wavenumber k_y according to the analytical expression [30]

$$\Delta' = 2 \frac{(3 + k_y^2)(5 - k_y^2)}{k_y^2 \sqrt{4 + k_y^2}}. \quad (22)$$

The tearing mode becomes unstable in nonideal MHD if $\Delta' > 0$, which is the case if $k_y < \sqrt{5}$. The field equations in EUTERPE are discretized in real space by a B-spline finite element method [31]. The y -direction is treated periodically, while the fields A and Φ are subject to Dirichlet boundary conditions with respect to x . For the simulations a resolution of up to 1024×128 grid points has been used for the x and y -direction, respectively. The code pushes the perturbed distribution function δf_s along particles trajectory using a Runge-Kutta-scheme of fourth order. In the gyrokinetic simulations no special initial perturbations are chosen so that the tearing instability evolves out of noise.

The gyrofluid code decomposes the fields into a time-independent background equilibrium and an evolving perturbation within a pseudospectral method [7]. Periodic boundary conditions are employed in both the x - and y -directions, and a grid of 1024×128 points has been used. Since periodic boundary conditions are imposed also along the x -direction, a Fourier series truncated to eleven modes is used to approximate Eq. (21). Finally, an Adams-Bashforth algorithm is applied to push the fields in time, and an initial disturbance on the

out-of-plane current density of width $\mathcal{O}(d_e)$ around the resonant surface is set to accelerate the onset of the tearing instability.

It is important to note that the boundary conditions for the fields with respect to the x -direction are different in the two codes. This is a consequence of the historical development of the codes. Due to the numerical method underlying the gyrofluid code periodic boundary conditions arise naturally. In EUTERPE the chosen field boundary conditions are fixed in the code. Our choice of the domain size in the x -direction is sufficient to avoid finite domain size effects on the value of the tearing stability index Δ' . However, in the following we will check the effects of the boundary conditions by performing a detailed linear benchmark with an eigenvalue approach. If, in the following, simulations in the drift kinetic limit were performed, this was achieved by setting the temperature ratio to $\tau = 1/900$, giving $\rho_i = 1/30 \ll d_e$, which makes the effect of the gyroaveraging operators negligible. Additionally, instead of the Padé approximation the long wavelength approximation was then used for the quasi-neutrality equation in EUTERPE.

III. LINEAR COMPARISON OF THE MODELS

As a first step we check the accuracy of the codes in the linear regime with a benchmark. For this purpose a numerical eigenmode and eigenvalue analysis is applied to each of the two models in the drift kinetic limit. After the accuracy of the codes is checked to a high degree, we proceed with a comparison of the models in both the drift kinetic limit and the finite Larmor radius case.

A. Eigenvalue equations

In this section we describe the procedure of performing a numerical benchmark using a shooting method to get the linear dispersion relation in the drift kinetic limit. An analysis of the eigenvalues and the eigenmode structure is given here for both the linearised gyrofluid and the gyrokinetic equations. The gyrofluid equations (14–20), and the gy-

rokinetic equations (5–9), are linearised using the ansatz $\delta\Phi(x, y, t) = e^{i(k_y y - \omega t)} \tilde{\Phi}(x)$ and $\delta A(x, y, t) = e^{i(k_y y - \omega t)} \tilde{A}(x)$ for the perturbed quantities, additionally assuming a long-wavelength approximation for the quasineutrality equation, Eq. (9). The field equations are cast into a general form with the coefficients q_j^i , with $(i, j) = (A, \Phi)$,

$$\frac{d^2 \tilde{\Phi}}{dx^2} = -q_\Phi^\Phi(x, \omega) \tilde{\Phi} - q_A^\Phi(x, \omega) \tilde{A} \quad (23)$$

$$\frac{d^2 \tilde{A}}{dx^2} = -q_\Phi^A(x, \omega) \tilde{\Phi} - q_A^A(x, \omega) \tilde{A} \quad (24)$$

The linearisation of the gyrofluid system gives the following coefficients

$$q_\Phi^\Phi(x, \omega) = -k_y^2 + \sum_s q_s \frac{F'_{0,s}}{N_s} \frac{k_y}{\omega} \quad (25)$$

$$q_A^\Phi(x, \omega) = \sum_s \frac{q_s}{N_s} \left(-q_s - \frac{k_s}{k_\parallel} N_s - \tau_s \rho_{S,e}^2 \frac{k_\parallel k_s}{\omega^2} \right) \quad (26)$$

$$q_\Phi^A(x, \omega) = \sum_s -\frac{F'_{0,s}}{N_s} \frac{k_y}{\omega} \quad (27)$$

$$q_A^A(x, \omega) = \sum_s \frac{q_s}{N_s} \left(-q_s - \tau_s \rho_{S,e}^2 \frac{k_\parallel k_s}{\omega^2} \right) \quad (28)$$

where the prime denotes the derivative with respect to x . Also the quantities

$$F'_{0,s} = -B_{y,0} + (-1)^{s+1} d_s^2 u'_{0,s} \quad (29)$$

$$k_\parallel = -A'_0 k_y \quad (30)$$

$$k_s = -u'_{0,s} k_y \quad (31)$$

$$N_s = d_s^2 \left(1 - \tau_s \frac{\rho_{S,e}^2}{d_s^2} \frac{k_\parallel^2}{\omega^2} \right), \quad (32)$$

have been introduced to make the notation more compact. Note that in the above relations $\tau_1 = \tau$ for ions and $\tau_2 = 1$ for electrons.

The coefficients resulting from the linearisation of the gyrokinetic model are

$$q_{\Phi}^{\Phi}(x, \omega) = -k_y^2 + \alpha^2 \beta_e \sum_s \frac{\Omega_s}{\mu_s} \frac{X_s}{v_s^2 k_{\parallel}} \langle V_s^1 \rangle \quad (33)$$

$$q_A^{\Phi}(x, \omega) = -\alpha \sqrt{\beta_e} \sum_s \frac{\Omega_s}{\mu_s} \frac{X_s}{v_s^2 k_{\parallel}} (\langle V_s^2 \rangle + u_{0,s} \langle V_s^1 \rangle) \quad (34)$$

$$q_{\Phi}^A(x, \omega) = n_e \sum_s \frac{\Omega_s}{\mu_s} \frac{X_s}{v_s^2 k_{\parallel}} (\langle V_s^2 \rangle + u_{0,s} \langle V_s^1 \rangle) \quad (35)$$

$$q_A^A(x, \omega) = -k_y^2 - \frac{n_e}{\alpha \sqrt{\beta_e}} \sum_s \frac{\Omega_s}{\mu_s} \times \left(\frac{X_s}{v_s^2 k_{\parallel}} (\langle V_s^3 \rangle + 2 u_{0,s} \langle V_s^2 \rangle + u_{0,s}^2 \langle V_s^1 \rangle) + \Omega_s \right). \quad (36)$$

where we have introduced $X_s = -k_s - k_{\parallel} \Omega_s$ and $\mu_i = 1, \mu_e = \mu$.

The functions $\langle V_s^n \rangle(x, \omega)$ for each species are defined as

$$\begin{aligned} \langle V_s^n \rangle &= \left(\sqrt{2} v_s \right)^{n-1} \frac{1}{\sqrt{\pi}} \int_{-\infty}^{\infty} dt t^n \frac{e^{-t^2}}{t - \left(\frac{1}{\sqrt{2} v_s} \left(\frac{\omega}{k_{\parallel}} - u_{0,s} \right) \right)} \\ &= \left(\sqrt{2} v_s \right)^{n-1} Z_n(\zeta_s) \end{aligned} \quad (37)$$

with $Z_n(\zeta_s)$ being the plasma dispersion function of n -th order with the species argument $\zeta_s = \left(\frac{\omega}{k_{\parallel}} - u_{0,s} \right) / (\sqrt{2} v_s)$.

These fourth-order equations are a nontrivial extension with respect to the case where the electrostatic potential $\tilde{\Phi}$ is neglected [14, 34], which is only of second order. Both these sets of eigenvalue equations are solved numerically using a shooting method, which is formulated as a Riccati problem [35]. By using an adaptive stepsize integrator results of very high accuracy results are obtained.

For the equilibrium configuration considered here, i.e. without any equilibrium gradients of temperature or density, the eigenvalue has only an imaginary part $\omega = i\gamma$. The Eqs. (23–24), with the coefficients (25–28) and (33–37), are solved using Dirichlet boundary conditions in x -direction.

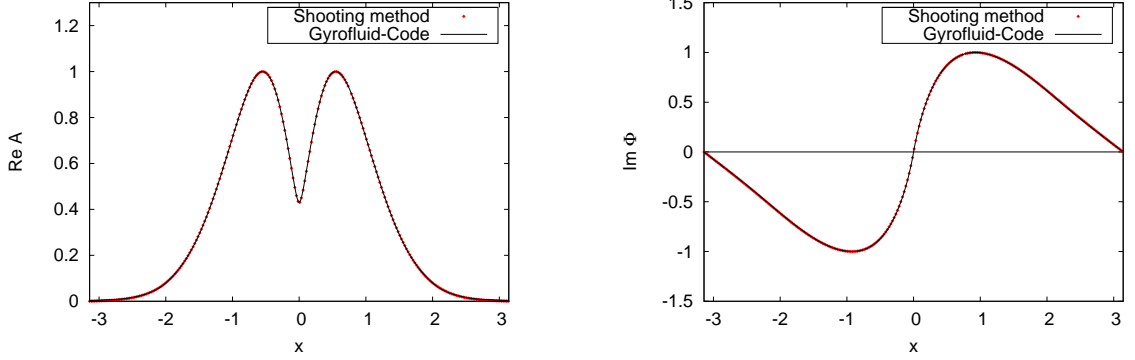


FIG. 1: Benchmark of the gyrofluid eigenfunctions. Left the real part of the parallel vector potential \tilde{A} , right the imaginary part of the electrostatic potential $\tilde{\Phi}$. Eigenfunctions are normalized by their maximum value.

B. Linear Benchmark with eigenvalue approach

The first benchmark is carried out for the parameter values $d_e = 0.1$, $d_i = 4.285$, $\rho_{S,e} = 0.6$, $k_y = 0.6$ using the drift kinetic limit. This corresponds to $\beta_e = 1.96 \cdot 10^{-2}$ and a realistic proton to electron mass ratio $\mu = 1836$. The comparison of the eigenfunction resulting from the shooting method with results from the gyrofluid simulation is shown in Figure 1. Due to symmetries of the equations and the pure imaginary eigenvalue, $\gamma = 0.0248$, only the real part of \tilde{A} remains, as well as only an imaginary part of $\tilde{\Phi}$. The field structures agree very well with results from the shooting code, although the boundary conditions with respect to x differ. The same procedure has been performed with EUTERPE using the coefficients defined by Eqs. (33–37). In this case $\gamma = 0.0273$, and both potentials are in good agreement with the results from the shooting method as well, as shown in Figure 2. In this case both methods used the same boundary conditions regarding the x -direction. The comparison with the solution of the gyrofluid problem shows that the instability is mainly influenced by the dynamics at the resonant layer. The solutions drop very fast to zero approaching the boundaries and therefore the influence of the boundary conditions is suppressed. This will be important for further nonlinear comparisons.

To check the eigenvalues over an extended k_y -spectrum of unstable modes, simulations have been performed with the previous setup varying the simulation domain size L_y . The

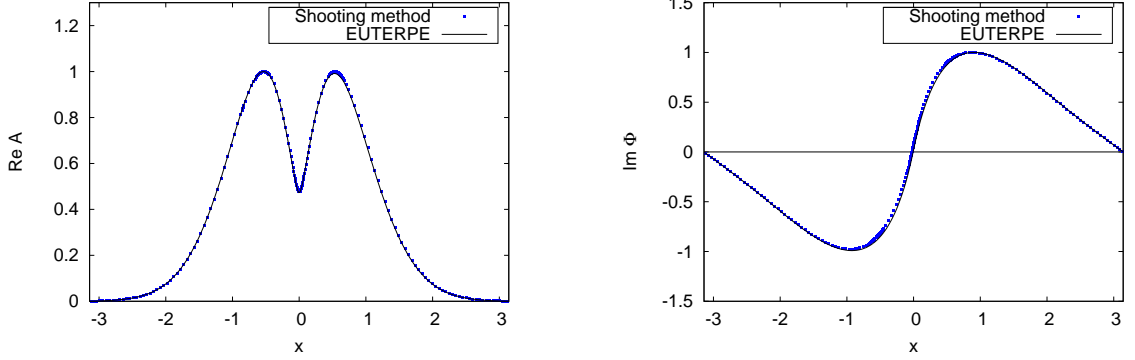


FIG. 2: Benchmark of the gyrokinetic eigenfunctions. Left the real part of the parallel vector potential \tilde{A} , right the imaginary part of the electrostatic potential $\tilde{\Phi}$. Eigenfunctions are normalized by their maximum value.

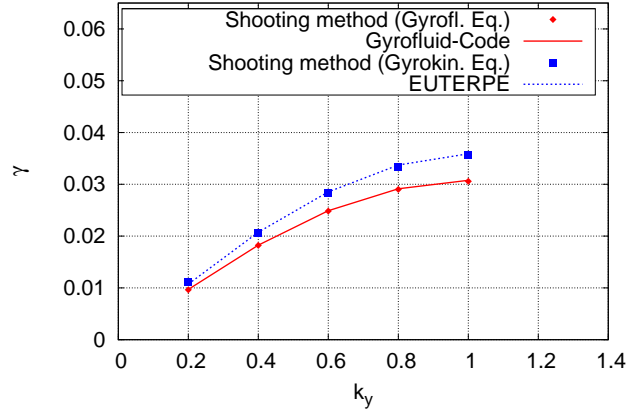


FIG. 3: A benchmark of the linear growth rates of both models for various wavevectors k_y . Both the gyrofluid code and gyrokinetic code work linearly exact.

comparison of both fluid and kinetic results and the relevant results of the shooting method are shown in Figure 3. We have thus shown numerically that the two codes give exact results in the linear regime over a wide range of k_y .

C. Model comparison in the drift kinetic limit

In the following we use two sets of parameters which are relevant for reconnection physics. The parameter associated with Setup I and II are listed in the Table below. Case

Setup	I	II
μ	1836	100
β_e	$4.91 \cdot 10^{-3}$	$4 \cdot 10^{-2}$
$\rho_{S,e}$	0.3	0.2
d_e	0.1	0.1
d_i	4.285	1.0

TABLE I: Set of parameters defining setup I and II used for the simulations.

I refers to a realistic mass ratio μ and "kinetic" regime, $\beta_e \gg m_e/m_i$, or equivalently $\rho_{S,e} \gg d_e$, whereas case II defines a "medium" range between kinetic and inertial regime, $\beta_e \sim m_e/m_i$.

Simulations for cases I and II have been performed for various k_y . Over the full range of wave numbers, from the large- Δ' to the small- Δ' cases, close to the stability threshold at $k_y \sim 2.23$, both models describe the reconnection process very well, as shown in Figure 4. It is found a relative maximum deviation of about 20% around $k_y \sim 1$ for both setups. However, in the small- Δ' limit the differences of the growth rates become smaller.

The kinetic description allows one to estimate the width of the region of particle acceleration, δ , due to the resonance condition $k_{\parallel} \rho_{S,e}/d_e = k_y \delta/l_s \cdot \rho_{S,e}/d_e \sim \gamma$ in the small- Δ' limit and $\delta \ll L$ [36]. This limit is defined by the condition $\Delta' d_e \ll (d_e/\rho_{S,e})^{1/3}$. Together with the kinetic dispersion relation in this limit, $\gamma = k_y d_e \rho_{S,e} \Delta'/l_s$, one gets the estimate $\delta \sim \Delta' d_e^2$. The two-fluid description also yields this scaling of the growth rate and current layer in the small- Δ' limit [17, 37].

Another point which might be important concerns the assumptions of the adopted gyrofluid model, which is a truncation of the much more complete model proposed by Snyder and Hammett [33]. The derivation uses the restriction that the bulk velocity of the species $u_{0,s}$ is much smaller than the thermal velocity v_s . Moreover, this model uses an unshifted Maxwellian when performing the integration over the velocity space to get the equations of moments. Therefore, the gyrofluid equations hold exactly only for

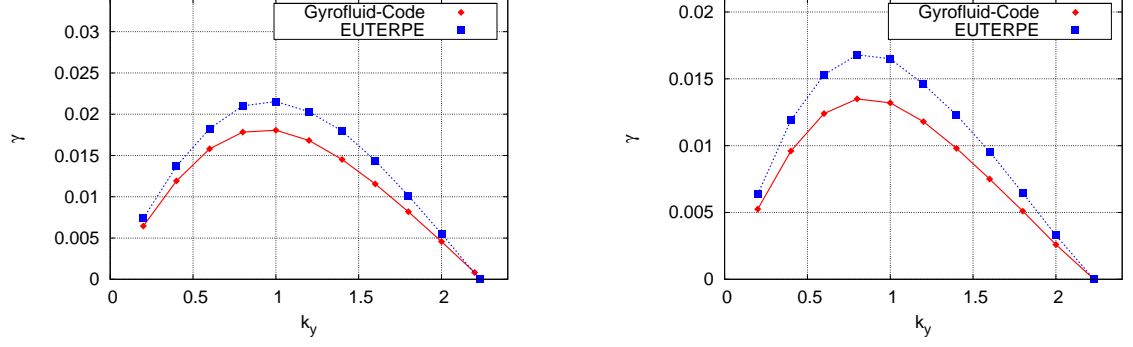


FIG. 4: The comparison of the linear dispersions shows a good agreement between the two approaches over the full k_y range. Left. Case I, $\mu = 1836$. Right. Case II, $\mu = 100$. (Solid lines connect the numerical results for better visualization.)

$C \ll 1$. For the linear simulations done here the amplitude of the sheared perpendicular field was chosen as $C = 0.1$, which approximates this limit very well and additionally allows relatively short simulation times. However we checked this point simulating a mode with $k_y = 1.0$, $d_e = 0.1$, $d_i = 4.285$, $\rho_{s,e} = 0.3$ and decreasing C from 10^{-1} to 10^{-4} . Although these runs required very long simulation times for small C , due to the dependence of γ from l_s , the relative deviation of the growth rates of the models fell from approximately 20% to 12%.

D. Influence of gyro-effects

It is desirable to go beyond the drift kinetic limit and simulate the tearing mode for finite ion temperatures when the gyroradius can become much larger than the thickness of the electron diffusion region which is $\mathcal{O}(d_e)$ [38]. Here we only compare the linear simulations of the codes using the setup scenario II for $k_y = 1.0$ and 2.0 , while varying τ . The gyrokinetic effects now enter according to Eq. (8) using the approximation of Padé.

Figure 5 shows that the growth rates obtained with the two different codes behave qualitatively very similar when we vary τ . While for small τ the growth rate remains nearly constant, for larger ion-gyroradii $\rho_i \gg \rho_{s,e}$ ($\tau \gtrsim 1$), the growth rate begins to increase

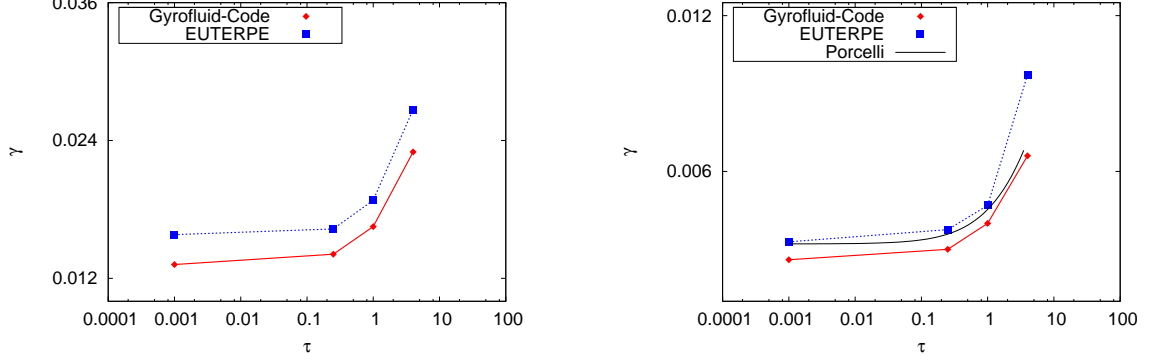


FIG. 5: In the medium- Δ' regime, $\Delta' d_e \sim 1$ (left), and in the small $\Delta' d_e$ regime (right) the codes show good agreement over whole range of τ . The analytical prediction, Eq. (38), fits well for both the gyrokinetic and gyrofluid model (right).

strongly.

For the medium range $k_y \sim 1$ both models cover the physics very well (Figure 5, left). This result is important since it proves clearly that the gyro-effects are being covered correctly by both gyro-approaches, which provides a good starting point for the following comparisons in the nonlinear regime.

The right frame of Figure 5 displays the simulation results in the small- Δ' limit, which for the case with hot electrons and ions is defined by $\Delta' d_e \ll [d_e / (\rho_{S,e} \sqrt{1 + \tau})]^{1/3}$. In this range of parameters an analytical prediction for a kinetic ion response together with an electron fluid derived by Porcelli gives [17]

$$\gamma = k_y \Delta' \sqrt{1 + \tau} \frac{d_e \rho_{S,e}}{l_s \pi}, \quad (38)$$

which reproduces the simulation results to high accuracy. Since the parallel ion dynamics and the gyrophase-independent part of the real space ion particle density $\langle n_i \rangle$ were neglected in Porcelli's theory, their effect plays a negligible role when considering an equilibrium without density gradients. Ion diamagnetic drifts may change this picture, and an investigation of nonuniform ion density equilibria will be the subject of a future publication.

IV. COMPARISON OF THE NONLINEAR MODELS

In fusion relevant applications the saturated behaviour of the tearing instability is a very important issue. Continuing with the parameters of both cases I and II we now discuss the nonlinear phase, concentrating on the small- Δ' regime. The saturated island half width w and oscillation frequency ω_B in the deeply nonlinear phase are the two most relevant observables. Up to now, in the literature there are only a few extended simulation results of these quantities in homogeneous plasmas [14, 15, 18].

It is important to note that the equilibrium considered in this section is unstable with respect to modes with $m = 1$, which can in general interact in the nonlinear phase with the $m = 0$ mode. Pseudospectral codes simulate a complete rectangular domain $[-m_{\max}, \dots, m_{\max}] \times [-n_{\max}, \dots, n_{\max}]$ in Fourier space [40], n being the mode number in z -direction ($n_{\max} = 0$ here), so the $m = 0$ mode is being simulated as well. In the gyrofluid simulations all relevant scales were well resolved by choosing the extent of the Fourier spectrum to $1/k_{\max} \ll d_e$. In EUTERPE it is not necessary to choose a corresponding domain setup. Nevertheless, to match the initial computational conditions of the two methods, EUTERPE was adjusted to adopt the filter $[-1, \dots, 1] \times [0]$. Because higher modes numbers $m = 2, 3, \dots$ are expected to play no role in the dynamics the chosen filter does not restrict the essential physics.

The gyrokinetic simulations were performed with up to $N_p = 3 \cdot 10^7$ markers with a minimum time step $\Delta t = 0.125$. The skin depth $d_e = 0.1$ is resolved with at least 16 points, whereas the width of the perturbed current produced by the parallel electric field, δ , was resolved with about ten points. The numerical resolution of the vector potential in the x -direction amounts to $n_x = 1024$ points, which separates scales up to $\Delta x = 5 \cdot 10^{-3}$. This introduces an upper error range, which can be removed with finer grid resolutions but demands a much higher computational effort.

We apply two different methods to obtain the island half widths w of the collisionless tearing

mode. Assuming the constant- \tilde{A} approximation, the half width evolution is given by [39]

$$w(t) = 2 \sqrt{\tilde{A}(x=0, y=0, t) l_s}. \quad (39)$$

Otherwise, without any approximation, we can obtain the exact island half width using the geometric definition of the island separatrix at each time step by solving numerically the equation

$$A(x=0, y=0, t) = A\left(x=w(t), y=\frac{\pi}{k_y}, t\right) \quad (40)$$

on the discrete spatial grid used in the codes. Assuming that the X -point is at $x=0, y=0$ and following the separatrix, the island half width w is found at $x=w(t), y=\pi/k_y$.

A. Drift kinetic limit

The evolution of the island half width into the deeply nonlinear regime is shown in Figure 6 for the parameters $k_y = 1.8$, $\mu = 1836$ and $\rho_{S,e} = 0.3$ obtained with both codes. This Figure shows the solution of Eq. (40) at each time step. Both gyrofluid and gyrokinetic models behave well in the nonlinear phase and show a clear saturated phase beginning at $t \sim 1500$. The energy conservation proved to be more accurate than 2.5%. Moreover, it turned out for all simulations presented here that the coupling between the $m=0$ and $m=1$ modes is very weak and can be neglected. Figure 7 shows a comparison of the evolution of the exact island half width and the island half width obtained according to Eq. (39) for the gyrofluid simulation shown in Figure 6. We have checked that for wavenumbers $k_y \geq 1.8$, which corresponds to the small- Δ' limit, the island half width calculated with the constant- \tilde{A} approximation is valid within the precision of measurement. Nevertheless, in the following we use Eq. (40).

When the island width becomes comparable to the linear current sheet thickness δ , the mode saturates [16]. After the transition into the saturation phase the width of the island begins to oscillate with a characteristic frequency ω_B , which is clearly visible in Figure 6 and 7. From the timeseries $w(t)$ the saturated island half width w is measured by taking

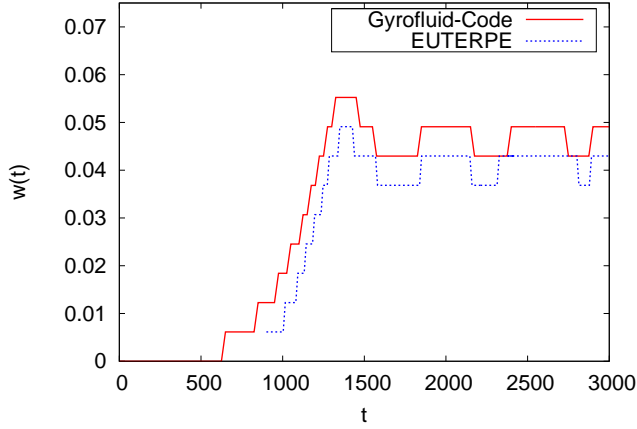


FIG. 6: Island half width as a function of time for setup I and $k_y = 1.8$. Both gyrofluid and gyrokinetic models show clear saturated behaviour of the mode. The steps are due to the spatial discrete grid points.

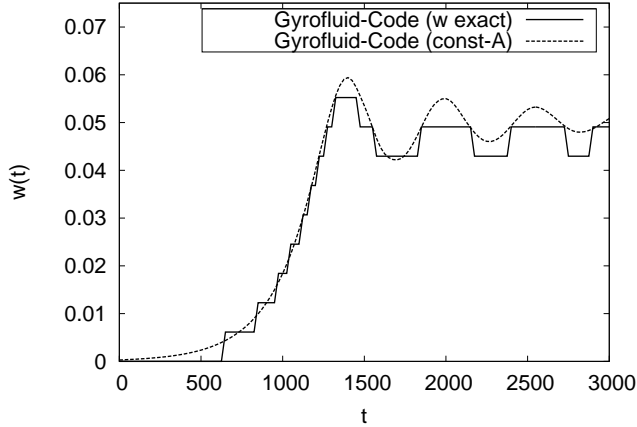


FIG. 7: Comparison between the exact island half width obtained by solving Eq. (40) on a discrete spatial grid and the island half width calculated according to Eq. (39) (Setup I and $k_y = 1.8$). In the small- Δ' limit the const- \tilde{A} approximation is numerically confirmed.

the mean value $w = \langle w(t) \rangle_T$ after saturation starts, with T indicating a period longer than the oscillation frequency.

In the following we measure both quantities w and ω_B for an extended parameter range to compare the gyrokinetic and gyrofluid models, and to check the validity of analytical predictions in this regime of parameters.

Figure 8 shows the saturated island half width w as a function of the longest wavelength

in the system for both parameter cases. For values $k_y \sim 1.6$ the relative difference of the island half widths obtained with the two adopted models is found to be about 30% for both parameter cases I and II. Increasing k_y to the range $k_y = 1.9 \dots 2.23$ close to the stability threshold the agreement between the results of the two codes is much better. The relative deviation of the island half widths is approximately 10% for $k_y = 1.9$ in both setups and vanishes practically for higher wavenumbers. This shows that for $\Delta' \lesssim 1$ both models agree very well. Therefore, there are no significant differences between the gyrofluid and the gyrokinetic models for small island widths, i.e. when $w \lesssim d_e$. So for the cases investigated here, in which the island half width and the current layer thickness δ are much smaller than the equilibrium scales, the fluid description produces practically the same island half widths as the more complete kinetic model. The comparison between the models also shows that the island width is slightly higher in the fluid description than in the kinetic model. These are the first extended comparisons of the saturated island width in slab geometry over a broad range of parameter.

Since for both parameter cases the ion skin depth is much larger than the electron skin

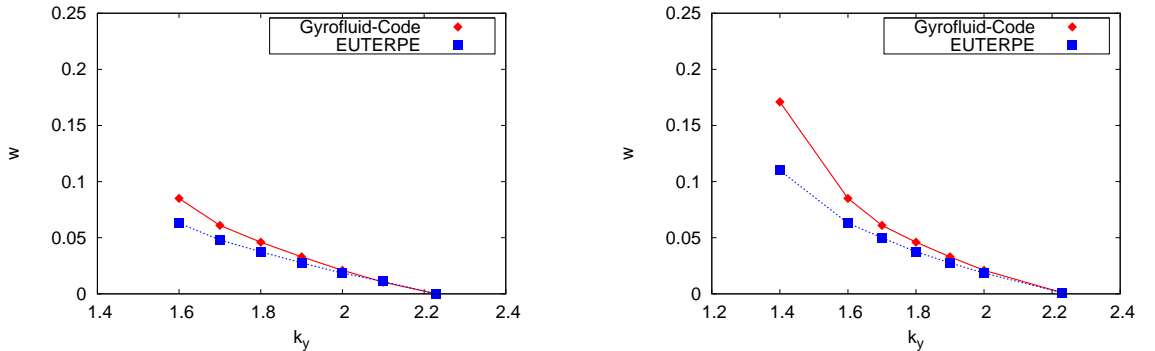


FIG. 8: Saturated island half width w as a function of k_y for Setup I (left panel) and for Setup II (right panel). The gyrokinetic and gyrofluid models show a very good agreement in determining the saturated island half width in the small- Δ' limit.

depth, $d_e \ll d_i$, electron inertia dominates completely. This regime has been investigated analytically in an early kinetic approach by Drake and Lee [16], where it was shown that the tearing mode saturates approximately when $w \sim \delta$, which in this regime means $w \sim \Delta' d_e^2$.

A more detailed estimation yields

$$w = \Delta' \frac{d_e^2}{2G} \quad (41)$$

with $G \sim 0.41$ [16]. Therefore, in the small island limit, $d_e \ll L \sim l_s$, the saturated island half width is described only by the skin depth d_e and the tearing mode stability parameter Δ' , which for our choice of the equilibrium is known analytically from Eq. (22).

The analytical prediction in comparison with our simulation results depending on k_y is shown in Figure 9. Eq. (41) well reflects the qualitative behaviour of w over the shown k_y -range, and agrees more closely with the gyrokinetic results than the gyrofluid ones. The deviations of the prediction of w can be caused by assumptions which are not completely valid in the simulations. For instance, in the analytical estimations the shifted background Maxwellian was not used rigorously, and in addition the density response was neglected.

For both parameter cases investigated here, the island width does not seem to depend on the values of $\rho_{S,e} = 0.2, 0.3$, as can be seen by comparing the left and right panels of Figure 8. This suggests that there is no influence of finite electron temperature effects on the island width. This is consistent with the fact that the analytical prediction, Eq. (41),

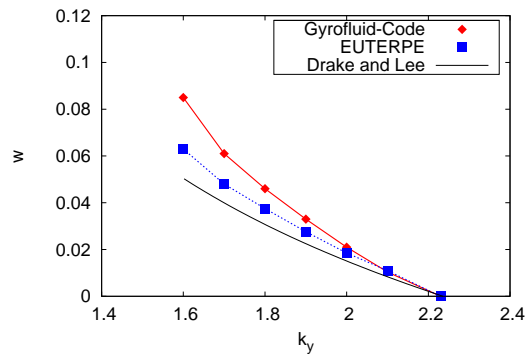


FIG. 9: The saturated island half width w depending on k_y is compared with the prediction by Drake and Lee [16] for the parameter case I. The analytical model shows a good qualitative agreement with simulation results for $\Delta' < 1$.

does not contain finite electron temperature effects related to $\rho_{S,e}$, which are linked to finite pressure effects and the width of the ion inflow region [37]. Since $\rho_{S,e}$ is comparable to the electron skin depth and the analytical model does not contain this quantity, it is unclear

whether it plays an important role in nonlinear simulations with both kinetic species. To investigate this dependence we fix the parameters $k_y = 1.8$, $\Delta' d_e \sim 0.25$, $\mu = 1836$ and vary $\rho_{s,e} = 0.3, 0.1, 0.05, 0.025$. The simulations have shown that the island half width remains the same ($w \sim 0.04$) to high accuracy in both gyrokinetic and gyrofluid simulations. It follows that in the small- Δ' regime the pressure scale has no influence on the saturation level of the collisionless tearing mode.

A further important nonlinear quantity which has been compared within the adopted gyrokinetic and gyrofluid models is the oscillation frequency ω_B that characterizes the saturation phase, as shown in Figures 6 and 7. In the kinetic context it was observed that this frequency is due to the bounce motion of trapped electrons in the island [14]. We consider again the parameter cases I and II, and measure the oscillation frequency as the mean value of several oscillation periods in the deeply nonlinear saturation phase, namely $\omega_B = 2\pi n_p / (T_f - T_i)$, being n_p the number of periods. In the gyrofluid simulations the

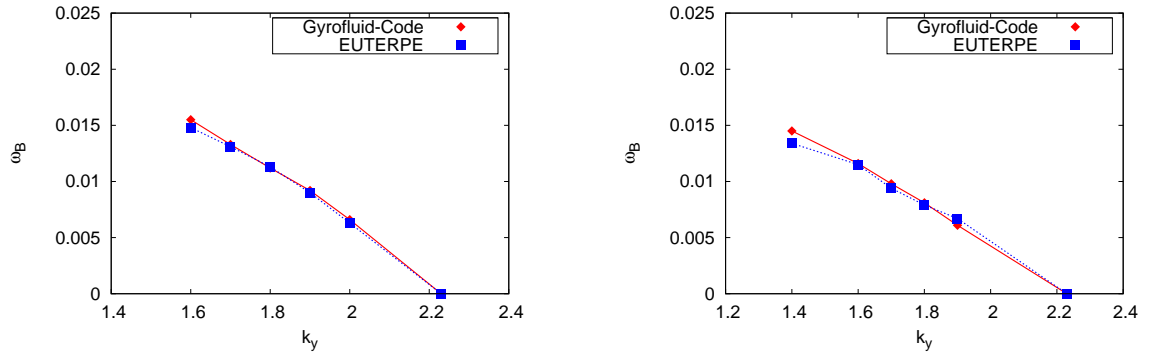


FIG. 10: Oscillation frequency as a function of the wavenumber k_y for the two models using the parameter setup I (left panel) and the parameter setup II (right panel). Both models deliver practically the same oscillation frequency in the saturated phase in the low- and medium- Δ' range.

oscillation frequency can always be clearly observed. While for parameters of case I the frequency can be measured clearly with the gyrokinetic code EUTERPE, this is more difficult in case II. Therefore, to obtain good results the number of markers was doubled to $N_p = 3 \cdot 10^7$ and the previous time step was halved to $\Delta t = 0.125$.

The results are displayed in Figure 10. The models agree very well for all wavenumbers k_y shown here, also for moderate values of $\Delta' \sim 1$. These results clearly show that also in this regime the oscillatory behaviour of the saturated reconnection process can be described completely by a fluid description.

From a rough kinetic estimation one gets $\omega_B \sim k_y v_e w / (2 l_s)$ [14, 16], so the frequency is roughly proportional to the island width and the stability parameter Δ' according to Eq. (41). The results in Figure 10 confirm this linear scaling in the limit of low Δ' values.

B. Finite ion temperature effects

This section deals with the extension of previous nonlinear results by including finite ion temperature effects using the full finite Larmor radius (FLR) response.

We focus on the parameter case I and investigate the behaviour of the saturated island half width and oscillation frequency with increasing ion temperature.

In Figure 11, left, the saturated island half width is shown when the ion temperature is

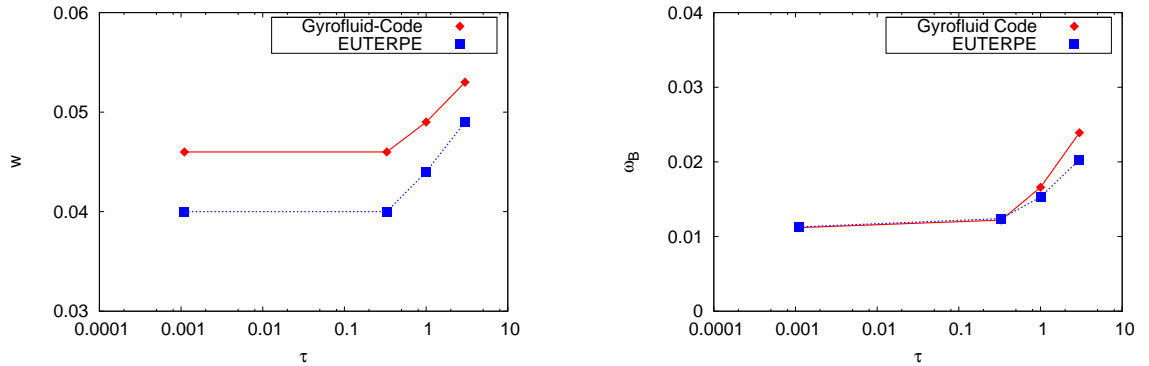


FIG. 11: Comparison of the island half width w (left panel) and the oscillation frequency ω_B (right panel) as a function of the temperature ratio τ for the parameter Setup I and $k_y = 1.8$.

varied using the values $\tau = 1/900, 0.25, 1, 4$ and fixing $k_y = 1.8$. The island width only changes by about 5% over approximately three orders of magnitude of τ . This shows that finite Larmor radius effects on w are weakly relevant for $\Delta' \lesssim 1$.

As stated earlier, Ref. [16] predicts the general saturation condition $w \sim \delta$. Here, due to the influence of finite ion temperature, the parallel current channel width changes according

to [20]

$$\delta \sim \frac{\gamma l_s}{k_y v_e \sqrt{1 + \tau}}. \quad (42)$$

On the other hand the growth rate increases according to $\gamma \propto \sqrt{1 + \tau}$, as we have seen in section III. Using Eq. (38) for the growth rate and Eq. (42) for the modified current width, the generalized scaling of the saturated island half width for finite τ becomes

$$w \sim \Delta' d_e^2 \quad (43)$$

as stated for the drift kinetic case. This estimation makes evident that the saturated island width does not change significantly with ion temperature.

In contrast to the island half width, the oscillation frequency changes significantly when the temperature ratio is varied, as shown in the right panel of Figure 11. The dependence of the oscillation frequency on the temperature ratio is similar to that of the growth rate. However, even with small but finite $\tau \lesssim 1$, the two models agree completely in the saturated phase.

V. SUMMARY

We have simulated collisionless magnetic reconnection via the tearing instability with a gyrokinetic and a gyrofluid model. The results of both approaches have been compared to each other linearly and nonlinearly for an extended set of parameters. To the best of our knowledge, this is the first comparison of these two models for simulations of the collisionless tearing mode.

As a first step, we have applied a shooting method to benchmark the linear simulations of both codes in the drift kinetic limit. The linear eigenmodes of the two models have been benchmarked for a single wave number and a fixed set of plasma parameters, whereas the linear growth rates of both codes have been compared for a range of wave numbers. It has been shown that in the linear regime both codes give results with high degree of accuracy. Then the results of the two models have been compared over the whole spectrum of linearly unstable wave numbers for two sets of plasma parameters showing a good agreement between the growth rates obtained with the gyrokinetic model and the gyrofluid one.

The linear simulations have been extended to the case of finite ion temperature, where we have shown that ion gyro-orbit averaging effects can be properly described by both approaches. Furthermore, numerical simulations in the small $\Delta'd_e$ range compare favorably with the asymptotic theory by Porcelli [17].

Nonlinear simulations of both models have been carried out in the small- Δ' regime. We have performed a detailed comparison of observables such as the evolution and saturation of the island width, as well as its oscillation frequency in the saturated phase, which has not been performed in this extend of parameter space so far. The gyrokinetic and gyrofluid simulations have shown that close to the marginal stability the evolution and saturation of the island width for both models is practically the same. Moreover, an important and new observation is that the oscillation frequency of the island width shows no difference between the two models. Therefore, the main result is that the nonlinear evolution of the collisionless tearing mode in the drift kinetic limit is essentially well described by

the fluid theory. We have also considered finite ion temperature effects in the saturated island phase. Here again both models differ only slightly when measuring the island width and its oscillation frequency. Therefore, in the regimes investigated here, the nonlinear reconnection physics can be completely described with a gyrofluid approach.

Slightly stronger deviations between the simulation results occur for $\Delta' \sim 1$, suggesting that further investigations will be of interest in this regime, as well as in cases where $\Delta' \gg 1$, for which a detailed nonlinear comparison between the gyrokinetic and gyrofluid models is still missing.

Acknowledgments

The authors would like to acknowledge fruitful discussions with Dario Borgogno and Alessandro Zocco. This work was supported by the European Community under the contracts of Association between Euratom and ENEA and by the Euratom research and training programme 2014–2018. Part of this work was carried out using the HELIOS supercomputer system at the Computational Simulation Centre of International Fusion Energy Research Centre (IFERC-CSC), Aomori, Japan, under the Broader Approach collaboration between Euratom and Japan, implemented by Fusion for Energy and JAEA. The views and opinions expressed herein do not necessarily reflect those of the European Commission.

-
- [1] M. Yamada, R. Kulsrud and H. Ji, *Rev. Mod. Phys.* **82**, 603 (2010).
 - [2] D. Grasso, F. Califano, F. Pegoraro and F. Porcelli, *Plasma Phys. Rep.* **26**, 512 (2000).
 - [3] N. F. Loureiro and G.W. Hammett, *J. Comput. Phys.* **227**, 4518 (2008).
 - [4] D. Grasso, E. Tassi and F. L. Waelbroeck, *Phys. Plasmas* **17**, 082312 (2010).
 - [5] E. Tassi, F. L. Waelbroeck and D. Grasso, *J. Phys.: Conf. Series* **260**, 012020 (2010).

- [6] D. Del Sarto, C. Marchetto, F. Pegoraro and F. Califano, Plasma Phys. Control. Fusion **53**, 035008 (2011).
- [7] L. Comisso, D. Grasso, E. Tassi and F. L. Waelbroeck, Phys. Plasmas **19**, 042103 (2012).
- [8] A. Biancalani and B. D. Scott, Europhys. Lett. **97**, 15005 (2012).
- [9] L. Comisso, F. L. Waelbroeck, and D. Grasso, J. Phys.: Conf. Ser. **401**, 012005 (2012).
- [10] L. Comisso, D. Grasso, F.L. Waelbroeck and D. Borgogno, Phys. Plasmas **20**, 092118 (2013).
- [11] F. L. Waelbroeck, Fusion Sci. Technol. **59**, 499 (2011).
- [12] W. Dorland and G. W. Hammett, Phys. Fluids B **5**, 812 (1993).
- [13] R. D. Sydora, Phys. Plasmas **8**, 1929 (2001).
- [14] W. Wan, Y. Chen and S. E. Parker, Phys. Plasmas **12**, 012311 (2005).
- [15] O. Zacharias, R. Kleiber and R. Hatzky, J. Phys.: Conf. Ser. **401**, 012026 (2012).
- [16] J. F. Drake and Y.C. Lee, Phys. Rev. Lett. **39**, 453 (1977).
- [17] F. Porcelli, Phys. Rev. Lett. **66**, 425 (1991).
- [18] X. Y. Wang, Y. Lin, L. Chen, X. Lu and W. Kong, Phys. Plasmas **18**, 122102 (2011).
- [19] J. M. TenBarge, W. Daughton, H. Karimabadi, G. G. Howes and W. Dorland, Phys. Plasmas **21**, 020708 (2014).
- [20] B. N. Rogers, S. Kobayashi, P. Ricci, W. Dorland, J. Drake, and T. Tatsuno, Phys. Plasmas **14**, 092110 (2007)
- [21] B. N. Rogers, S. Kobayashi, P. Ricci, W. Dorland, J. Drake, and T. Tatsuno, Phys. Plasmas **18**, 049902 (2011).
- [22] R. Numata, W. Dorland, G. G. Howes, N. F. Loureiro, B. N. Rogers and T. Tatsuno, Phys. Plasmas **18**, 112106 (2011).
- [23] M. J. Püschel, F. Jenko, D. Told, and J. Büchner, Phys. Plasmas **18**, 112102 (2011).
- [24] A. Mishchenko and A. Zocco, Phys. Plasmas **19**, 122104 (2012)
- [25] R. Kleiber, C. Beidler, M. Borchardt, T. Fehér, R. Hatzky, K. Kauffmann, A. Könies, A. Mishchenko and J. M. Garcia-Regaña, Proceedings of the 24th IAEA Fusion Energy Conference (2012), TH/P3-06.
- [26] T. S. Hahm, W. W. Lee and A. J. Brizard, Phys. Fluids **31**, 1940 (1988).
- [27] T. S. Hahm, Lu Wang and J. Madsen, Phys. Plasmas **16**, 022305 (2009).
- [28] R. Hatzky, A. Könies and A. Mishchenko, J. Comp. Phys. **225**, 568 (2007).
- [29] H. P. Furth, J. Killeen, and M. N. Rosenbluth, Phys. Fluids **6**, 459 (1963).

- [30] F. Porcelli, D. Borgogno, F. Califano, D. Grasso, M. Ottaviani and F. Pegoraro, Plasma Phys. Control. Fusion **44**, 389 (2002).
- [31] R. Hatzky, T. M. Tran, A. Könies, R. Kleiber and S. J. Allfrey, Phys. Plasmas **9**, 898 (2002).
- [32] F. L. Waelbroeck and E. Tassi, Commun. Nonlinear Sci. Numer. Simulat. **17**, 2171 (2012).
- [33] P. B. Snyder and G.W. Hammett, Phys. Plasmas **8**, 3199 (2001).
- [34] I. Katanuma and T. Kamimura, Phys. Fluids **23**, 2500 (1980).
- [35] M. R. Scott, J. Comp. Phys. **12**, 334 (1973).
- [36] J. F. Drake and Y. C. Lee, Phys. Fluids **20**, 1341 (1977).
- [37] A. Zocco and A. A. Schekochihin, Phys. Plasmas **18**, 102309 (2011).
- [38] S. C. Cowley, R. M. Kulsrud and T. S. Hahm, Phys. Fluids, **29**, 10 (1985).
- [39] R. J. Goldston and P. H. Rutherford, *Introduction to Plasma Physics* (Institute of Physics Publishing, Bristol and Philadelphia, 1995).
- [40] S. K. Lele, J. Comp. Phys. **103** (1992).